Research Square

Preprints are preliminary reports that have not undergone peer review.
They should not be considered conclusive, used to inform clinical practice,
or referenced by the media as validated information.

Fabrication of polyaniline-encapsulated ammonium vanadate for high-performance aqueous zinc-ion storage

Jiacheng Huang
Huai'an University
Xiaoran Guo
Huai'an University
Menglong Zhu
Huai'an University
Xiaojie Zhang
xjzhang@hau.edu.cn
Huai'an University
Xuan Zhao
Huai'an University
Ruiwen Tang
Huai'an University
You Qi
Huai'an University
Xiaoyan Gao
Huai'an University
Yong Yang
Huai'an University
Yuyu Sun
Huai'an University

Research Article

Keywords: Aqueous zinc-ion batteries, Polyaniline coating, Interfacial engineering, Ammonium vanadate

Posted Date: November 3rd, 2026

DOI: https://doi.org/10.21203/rs.3.rs-11246497/v1

License: This work is licensed under a Creative Commons Attribution 4.0 International License.
Read Full License

Additional Declarations: No competing interests reported.

Abstract

Aqueous zinc-ion batteries (AZIBs), which combine non-flammable aqueous electrolytes with low cost and environmental compatibility, hold considerable promise for grid-scale energy storage. Layered vanadium oxides stand out among the cathode candidates considered so far, since their open framework structures, high theoretical capacities, and abundant vanadium reserves are well suited to Zn^{2+} storage. In practice, however, these electrodes suffer from poor electronic conductivity and progressive vanadium loss during cycling, and water at the electrode–electrolyte contact further accelerates this degradation. In this work, polyaniline (PANI) was anchored on the surface and intercalated into the interlayer galleries of ammonium vanadate ($NH_4V_4O_{10}$, NVO), yielding NVO@PANI composites. The hydrophobic PANI layer shields the electrode surface from water, suppresses vanadium dissolution, and thereby extends cycle life, while the conductive polymer network simultaneously boosts electron transport and rate capability. In addition, PANI incorporation partially amorphizes the NVO lattice, generating extra pathways for Zn2 + migration and accelerating ion diffusion. The optimal NVO@PANI-50 cathode achieves 443.68 mAh g^{-1} at 0.2 A g^{-1} and 255.99 mAh g^{-1} at 5 A g^{-1}, with 93.92% of the initial capacity retained after 1000 cycles. This interfacial-engineering strategy thus provides a scalable pathway toward robust vanadium-based cathodes for AZIBs.

1 Introduction

Lithium-ion batteries (LIBs), though still preferred for portable electronics and electric vehicles owing to their high energy density, long lifespan, and elevated operating voltage, are ill-suited to large-scale storage because of limited lithium resources, high cost, and the safety hazards posed by organic electrolytes [1, 2]. Rechargeable aqueous zinc-ion batteries (AZIBs) have accordingly attracted growing interest as an alternative energy-storage technology [3]. Zinc is abundant, inexpensive, and nontoxic; water-based electrolytes largely eliminate flammability and toxicity concerns; and the Zn/Zn^{2+} redox couple delivers a high theoretical capacity (820 mAh g^{-1}) at a favorable reduction potential [4, 5]. Still, the cathode remains the main constraint on AZIB development, since it determines energy density, rate capability, and cyclability. Among the cathode families reported to date—manganese oxides [6], Prussian blue analogues [7], organic materials [8], and vanadium compounds [9]—layered vanadium-based oxides are especially attractive due to their multiple valence states, open frameworks, and favorable operating voltages [10]. Their inherently low electronic conductivity, however, restricts charge transfer and Zn^{2+} diffusion, limiting capacity and rate performance [11].

Various strategies, including morphology engineering [12], composite construction [13], and heteroatom doping [14], have been used to improve the electrochemical properties of vanadium-based cathodes. For example, Yang and co-workers prepared VO_2(D) hollow nanospheres via template-free hydrothermal synthesis [15], the hollow structure shortened Zn^{2+} diffusion paths and gave 408 mAh g^{-1} at 0.1 A g^{-1} and 200 mAh g^{-1} at 20 A g^{-1}. Yet while nanoscale structuring and porosity shorten ion-diffusion distances, the accompanying large surface area can aggravate vanadium dissolution, H^+ co-

intercalation, and side-product deposition, ultimately compromising long-term durability. As reported by Huang and co-workers, carbon-coated $Na_3V_2(PO_4)_3$ nanoparticles ($Na_3V_2(PO_4)_3$/C) exhibited an initial discharge capacity of 97 mAh g^{-1} at 0.5 C, which dropped to only 72 mAh g^{-1} after 100 cycles (74% retention) [16]. Cation doping—for instance with K^+, Mn^{2+}, and Ba^{2+} incorporation, can modulate the electronic structure of the host and facilitate charge/ion conduction [17–19]. Over-doping, on the other hand, risks lattice distortion, structural collapse, side reactions, and metal leaching [20]. Beyond such bulk-level modification, the cathode-electrolyte interface plays a decisive role in the final electrochemical output, and hydrophobic interfacial layers have proven effective in restraining electrolyte-induced vanadium corrosion [21, 22]. However, most existing strategies address only a single deficiency and rarely reconcile structural stability, interfacial passivation, and electronic conduction at the same time. An interfacial design that combines kinetic acceleration with structural reinforcement is therefore highly desirable.

In this study, a polyaniline-wrapped ammonium vanadate composite (NVO@PANI) was prepared via a facile one-step hydrothermal route. The conductive PANI shell upgrades the electronic conductivity of the hybrid and, in turn, its rate performance. Beyond this, PANI incorporation triggers partial amorphization of $NH_4V_4O_{10}$, opening up additional ion-transport channels and quickening Zn^{2+} diffusion. The polymer sheath also serves as a protective layer that curbs the dissolution of vanadium species during charge/discharge cycling, thereby reinforcing both structural and interfacial stability. As a result, the optimized NVO@PANI-50 electrode delivers 443.68 mAh g^{-1} at 0.2 A g^{-1} and still retains 255.99 mAh g^{-1} after 1000 cycles at 5 A g^{-1} (93.92% retention). These findings underline the promise of PANI-assisted interfacial engineering for constructing durable, high-rate vanadium-based cathodes.

2. Experimental

In a typical process, NH_4VO_3 (0.2428 g) was first dissolved in deionized water (35 mL) with magnetic stirring for 10 min. $H_2C_2O_4$ (0.2622 g) and a predetermined quantity of aniline were subsequently introduced into the solution. The mixed precursor was transferred to a 50 mL Teflon-lined stainless-steel autoclave and heated at 180°C for 3 h. After the autoclave had cooled to room temperature, the solid product was collected by centrifugation, rinsed several times with deionized water and ethanol, and finally dried at 60°C for 12 h. Varying the aniline dosage yielded the composites denoted NVO@PANI-30, NVO@PANI-50, and NVO@PANI-70, while bare NVO was synthesized under identical conditions in the absence of aniline.

Crystallographic information was acquired on a Bruker D8 Discover diffractometer operated with Cu Kα radiation (λ = 0.15406 nm). The surface chemical states were probed by X-ray photoelectron spectroscopy (XPS, Thermo Scientific K-Alpha), and electron paramagnetic resonance (EPR) data were collected on a Bruker A300 spectrometer. Raman spectra were obtained with a Thermo Fisher DXR confocal micro-Raman system under 532 nm laser excitation. Particle morphology and microstructure were examined by scanning electron microscopy (SEM, FEI FEG250) and transmission electron

microscopy (TEM, FEI Talos F200S). Contact-angle measurements were performed on a KRÜSS GmbH DSA25 analyzer to assess surface wettability, and elemental concentrations were quantified by inductively coupled plasma-optical emission spectrometry (ICP-OES, OPTIMA 7000DV).

To prepare the working electrodes, the active material, Super P, and PVDF were blended in NMP at a weight ratio of 7:2:1. The homogenized slurry was spread onto stainless-steel foil and dried under vacuum at 100°C for 12 h, giving an active-material loading of 1–2 mg cm^{-2}. CR2025 coin cells were then assembled in ambient atmosphere with Zn foil (99.99%) as the anode, Whatman GF/A glass-fiber paper as the separator, and 3 mol L^{-1} $Zn(OTF)_2$ as the electrolyte. Cyclic voltammetry (CV) and electrochemical impedance spectroscopy (EIS, 0.01 Hz–100 kHz) were performed on a Donghua DH7000C workstation, whereas galvanostatic charge/discharge (GCD) and galvanostatic intermittent titration technique (GITT) measurements were conducted on a Neware CT-4008 Tn battery tester.

3. Results and discussion

The XRD patterns of NVO@PANI-30, NVO@PANI-50, and NVO@PANI-70 are displayed in Fig. 1a, match the reference pattern of NVO (JCPDS No. 31–0057) [23]. Relative to pristine NVO (Fig. S1), the modified composite samples show attenuated diffraction intensities and enlarged full widths at half maximum, pointing to a loss of crystallinity. As the aniline content rises, the reflections of NVO@PANI-50 and NVO@PANI-70 move slightly toward smaller angles. This low-angle shift is ascribed to the intercalation of PANI-related species into the interlayer galleries of NVO during synthesis, which widens the interlayer spacing, generates localized structural disorder, and ultimately favors partial amorphization [24].

Figure 1b compares the Raman spectra of NVO and NVO@PANI-50. The Raman shift bands at 154 and 272 cm^{-1} in low-wavenumber range originate mainly from framework vibrations of the vanadate lattice, encompassing V–O–V and V = O modes [9]. The signals at 425, 519, and 694 cm^{-1} are attributable to the bending, symmetric stretching, and asymmetric stretching vibrations of V-O-V bonds, respectively [25]. Upon PANI modification, extra scattering features emerge in 1100–1600 cm^{-1} window, which are fingerprint singals of the polyaniline backbone involving C–H, C–N, C = N, and aromatic C = C vibrations, their emergence verifies that the polymer is well retained in the composite. More specifically, the peak at 1169 cm^{-1} corresponds to C-H vibration, while the peaks at 1345 and 1493 cm^{-1} originate from C-N and C = N stretching vibrations, respectively. The band at 1555 cm^{-1} reflects the skeletal vibration of C = C within the benzene ring [26]. These polymer-derived bands collectively confirm that polyaniline has been successfully incorporated. EPR spectroscopy was then employed to probe the defect chemistry of the electrodes (Fig. 1c). Unlike bare NVO, each NVO@PANI sample exhibits a pronounced oxygen-vacancy resonance whose intensity scales with the aniline dosage; oxygen vacancies are widely recognized to promote electronic transport and accelerate electrochemical reaction kinetics [27]. Meanwhile, the PANI coating itself establishes a conductive network that further upgrades the overall electronic conductivity of the composite.

SEM inspection (Fig. 2a–c) reveals that, relative to pristine NVO (Fig. S2), PANI nanoparticles are evenly anchored over the NVO nanosheet surfaces in the NVO@PANI composites, evidencing successful polymer encapsulation. The TEM image of NVO@PANI-50 (Fig. 2d) likewise shows polymer particles dispersed homogeneously on the sheet surface, and high-resolution TEM (Fig. 2e) discloses a largely disordered lattice consistent with the diffuse rings of the selected-area electron diffraction pattern [28]. Energy-dispersive X-ray spectroscopy (EDS) elemental mapping (Fig. 2f) confirms the homogeneous distribution of C, N, O, and V, with mass fractions of 12.56%, 4.48%, 56.13%, and 26.83%, respectively. The combined intercalation and surface coating of PANI disrupt the long-range ordering of the NVO lattice, giving rise to a pronounced amorphous character [29]. This structural disorder furnishes abundant channels for ion transport, easing Zn^{2+} migration and thereby enhancing electrochemical kinetics and energy-storage capability [30].

The contact-angle data collected in Fig. 3a reveal that PANI modification flips the surface wettability of NVO from hydrophilic to hydrophobic. Bare NVO gives a contact angle of 64.5°, typical of a hydrophilic surface, whereas after polymer encapsulation the values rise to 106.5°, 117.5°, and 120.0° for NVO@PANI-30, NVO@PANI-50, and NVO@PANI-70, respectively—clear evidence that the PANI layer markedly enhances surface hydrophobicity [31]. The chemical stability of the electrodes in the electrolyte was then assessed by soaking NVO and the NVO@PANI samples in 3 M $Zn(OTF)_2$ for 30 days and measuring the leached vanadium by ICP-OES (Fig. 3b). The electrolyte in contact with pristine NVO contained 108.2 mg L^{-1} of vanadium, while the values for NVO@PANI-30, NVO@PANI-50, and NVO@PANI-70 dropped sharply to 36.4, 28.7, and 25.1 mg L^{-1}, respectively. These outcomes confirm that the PANI coating efficiently restrains vanadium dissolution and preserves the structural integrity of the electrode during operation [32].

XPS was employed to characterize the surface composition and chemical states of NVO@PANI-50. The survey spectrum (Fig. 4a) displays O 1s, V 2p, N 1s, and C 1s signals, and the N 1s feature near 401 eV evidences the surface presence of PANI. Deconvolution of the V 2p envelope yields four components at 524.88, 523.37, 517.29, and 515.84 eV, assigned to V^{5+} 2p1/2, V^{4+} 2p1/2, V^{5+} 2p3/2, and V^{4+} 2p3/2, respectively, confirming a mixed-valence vanadium environment. The subtle peak displacements relative to pristine NVO indicate that the PANI layer perturbs the local electronic surroundings of vanadium [33]. In the C 1s region (Fig. 4c), three components located at 284.40, 285.20, and 287.40 eV can be ascribed to C = N, C–N, and C = C species of PANI, respectively. The N 1s spectrum (Fig. 4d) is resolved into a peak at 399.40 eV from imine nitrogen (–N=) and two peaks at 400.15 and 401.17 eV from amine nitrogen (–NH–) and positively charged nitrogen ($–N^{+}–$), respectively. Together, these observations corroborate the successful PANI coating and delineate the local electronic states of the composite.

Figure 5a shows the first three CV sweeps of the NVO@PANI-50 electrode at 0.2 mV s^{-1}. A single dominant redox couple is evident, implying that the PANI coating leaves the intrinsic redox chemistry of the NVO cathode unaltered, which proceeds mainly through V^{5+}/V^{4+} or V^{5+}/V^{3+} conversions. The galvanostatic profiles (Fig. 5b) exhibit well-defined charge/discharge plateaus that coincide with the CV

peaks, and their similarity across current densities testifies to highly reversible Zn^{2+} (de)insertion. Among the tested electrodes, bare NVO delivers the lowest capacities (Fig. S3), whereas NVO@PANI-50 shows the best rate behavior (Fig. 5c), attaining 443.68, 413.47, 379.04, 348.28, 313.53, and 278.67 mAh g^{-1} as the current density rises from 0.2 to 5 A g^{-1}, all surpassing the values recorded for NVO@PANI-30 and NVO@PANI-70. The relatively weak performance of NVO@PANI-70 likely stems from its overly thick PANI layer, which lowers the fraction of electrochemically active material and impedes efficient ion transport [34]. An intermediate PANI loading is therefore required to strike a balance between dissolution suppression and capacity delivery. Under prolonged cycling at 5 A g^{-1} (Fig. 5d), NVO@PANI-50 preserves 93.92% of its initial capacity over 1000 cycles, underscoring its outstanding cyclability; in contrast, bare NVO retains below 100 mAh g^{-1} at 2 A g^{-1} over 500 cycles (Fig. S4).

To gain deeper insight into the reaction kinetics of NVO@PANI-50, CV scans were recorded at sweep rates spanning 0.2–1.0 mV s^{-1} (Fig. 6a). As the sweep rate increases, the redox peaks drift progressively, a consequence of stronger electrode polarization [4]. The charge-storage behavior can be analyzed using the power-law dependence of the peak current (i) on the scan rate (v):

$$i = av^b \quad (1)$$

Taking logarithms, Eq. (1) can be rewritten as log(i) = b log(v) + log(a), with a and b serving as adjustable constants; the slope b is obtained by linearly fitting log(i) against log(v). A b value near 0.5 signifies a diffusion-controlled process, while a value approaching 1.0 denotes surface-capacitive behavior [35]. Intermediate b values ($0.5 < b < 1$) indicate that charge storage is co-governed by diffusion-limited insertion and pseudocapacitive reactions. From the fits in Fig. 6b, the b values for Peaks 1 and 2 are 0.76 and 0.62, respectively, establishing that Zn^{2+} storage in NVO@PANI-50 combines battery-type and pseudocapacitive contributions.

$$i = k_1v + k_2v^{1/2} \quad (2)$$

$$i/v^{1/2} = k_1v^{1/2} + k_2 \quad (3)$$

Equations (2) and (3) were then applied to separate the capacitive and diffusion contributions at each scan rate. In this framework, the total current (i) is decomposed into a capacitive component (k_1v) and a diffusion-controlled contribution ($k_2v^{1/2}$), where k_1 and k_2 are the corresponding coefficients. For convenience, Eq. (3) can be rearranged into the linear form given in Eq. (4). As summarized in Fig. 6c, the capacitive contribution ratios of NVO@PANI-50 increase from 56% to 61%, 67%, 75%, and 81% as the scan rates steps from 0.2 through 1.0 mV s^{-1}, consistently exceeding those of pristine NVO (Fig. S5). The growing capacitive share at faster sweep rates points to accelerated surface/near-surface charge storage, which corroborates the superior rate capability seen in the GCD measurements and underscores the pivotal role of pseudocapacitance in high-rate energy storage [36].

Galvanostatic intermittent titration technique (GITT) was additionally applied to track the Zn^{2+} diffusion kinetics of NVO@PANI-50 (Fig. 6d, 6e). The derived diffusion coefficient D_{Zn}^{2+} stays within 10^{-10} to 10^{-8} $cm^2\ s^{-1}$ over the full charge/discharge course, well above the values of pristine NVO, confirming that PANI introduction markedly facilitates Zn^{2+} migration and diffusion [24]. Beyond the kinetic benefit, the partial intercalation of PANI and the accompanying transformation of the host into an amorphous structure furnish more abundant diffusion pathways, accelerating zinc-ion transport and thereby expediting the overall electrode reaction. Electrochemical impedance spectroscopy (EIS) further confirmed the favorable influence of the PANI coating on interfacial resistance: as shown in Fig. 6f, the charge-transfer resistances (Rct) of NVO@PANI-30, NVO@PANI-50, and NVO@PANI-70 are 50.18 Ω, 38.27 Ω, and 43.32 Ω, respectively, all markedly lower than the 92.34 Ω obtained for pristine NVO. The conductive PANI layer thus enhances the overall electrical conductivity and accelerates electrode reaction kinetics [14, 22].

4. Conclusion

In summary, NVO@PANI composites were successfully prepared and validated as cathode materials for AZIBs. The incorporation of PANI partially amorphizes the NVO host, creating supplementary channels for Zn^{2+} migration, while the conductive polymer coating simultaneously elevates electronic conductivity and boosts rate capability. More critically, the hydrophobic PANI sheath curbs vanadium dissolution and reinforces cycling stability. The optimized NVO@PANI-50 electrode delivers 443.68 mAh g^{-1} at 0.2 A g^{-1} and maintains 255.99 mAh g^{-1} after 1000 cycles at 5 A g^{-1}, equivalent to 93.92% capacity retention. By coupling interfacial protection, conductivity enhancement, and structural-disorder engineering within a single design, this work charts a practical route toward durable, high-rate vanadium-based cathodes for aqueous zinc-ion batteries.

CRediT authorship contribution statement

Jiacheng Huang: Data curation; Writing – original draft. Xiaoran Guo: Data curation; Writing – original draft. Menglong Zhu: Methodology; Software; Writing – original draft. Xiaojie Zhang: Conceptualization; Supervision, Project administration. Xuan Zhao: Formal analysis. Ruiwen Tang: Data curation; Formal analysis. You Qi: Data curation; Formal analysis. Data curation. Xiaoyan Gao: Data curation; Formal analysis. Yong Yang: Resources; Writing – review & editing. Yuyu Sun: Formal analysis.

Declarations

Declaration of competing interest

The authors declare that they have no known competing financial interests or personal relationships that could have appeared to influence the work reported in this paper.

Author Contribution

Jiacheng Huang: Data curation; Writing – original draft. Xiaoran Guo: Data curation; Writing – original draft. Menglong Zhu: Methodology; Software; Writing – original draft. Xiaojie Zhang: Conceptualization; Supervision, Project administration. Xuan Zhao: Formal analysis. Ruiwen Tang: Data curation; Formal analysis. You Qi: Data curation; Formal analysis. Data curation. Xiaoyan Gao: Data curation; Formal analysis. Yong Yang: Resources; Writing – review & editing. Yuyu Sun: Formal analysis.

Acknowledgements

This work was supported by the Natural Science Foundation of Huai'an University (23HGZ012), Opening Fund of National & Local Joint Engineering Research Center for Deep Utilization Technology of Rock-salt Resource (No. SF202416), Major Program of Natural Science Foundation of the Higher Education Institutions of Jiangsu Province of China (No. 24KJA430008).

Data availability

Data will be made available on request.

References

1. Y. Li, S. Kumar, G. Yang, J. Lu, Y. Yao, K. Kang, Z.W. Seh, The contrast between monovalent and multivalent metal battery anodes, Science, 389 (2025) eadl5482.
2. J. Xu, J. Zhang, T.P. Pollard, Q. Li, S. Tan, S. Hou, H. Wan, F. Chen, H. He, E. Hu, K. Xu, X.-Q. Yang, O. Borodin, C. Wang, Electrolyte design for Li-ion batteries under extreme operating conditions, Nature, 614 (2023) 694–700.
3. Y. Dong, H. Hu, P. Liang, L. Xue, X. Chai, F. Liu, M. Yu, F. Cheng, Dissolution, solvation and diffusion in low-temperature zinc electrolyte design, Nature Reviews Chemistry, 9 (2025) 102–117.
4. M. Liu, X. Li, M. Cui, F. Chen, J. Li, W. Shi, Y. Liu, X. Li, Y. Wang, W. Zhang, C. Shao, Y. Liu, Amorphous organic-hybrid vanadium oxide for near-barrier-free ultrafast-charging aqueous zinc-ion battery, Nature Communications, 15 (2024) 10769.
5. H. Hao, K. Chen, H. Liu, H. Wang, J. Liu, K. Yang, H. Yan, A Review of the Positive Electrode Additives in Lead-Acid Batteries, International Journal of Electrochemical Science, 13 (2018) 2329–2340.
6. Y. Long, X. Zhang, M. Zhu, X. Gao, Z. Liu, S. Chen, J. Pang, Rational design of α-MnO2@ TiO2 composites for high-performance zinc ions batteries, Journal of Energy Storage, 103 (2024) 114328.
7. Y. Tan, H. Yang, C. Miao, Y. Zhang, D. Chen, G. Li, W. Han, Hydroxylation strategy unlocking multi-redox reaction of manganese hexacyanoferrate for aqueous zinc-ion battery, Chemical Engineering Journal, 457 (2023) 141323.

8. Z. Luo, Z. Liu, H. He, Z. Zhang, Y. Chen, C. Peng, J. Zeng, Suppressing the dissolution of vanadium by organic-inorganic hybrid for aqueous zinc-ion batteries, Journal of Materials Science & Technology, 145 (2023) 93–100.
9. M. Zhu, I. Ullah, X. Zhang, Y. Long, X. Gao, Z. Liu, Y. Yang, G. Shen, Phenolphthalein-Modified Multivalent Vanadium Oxide: Harnessing Oxygen Vacancies and Hydrophobicity for Improved Aqueous Zinc-Ion Battery Performance, ACS Sustainable Chemistry & Engineering, 12 (2024) 4255–4263.
10. Z. Liu, Y. Huang, Y. Huang, Q. Yang, X. Li, Z. Huang, C. Zhi, Voltage issue of aqueous rechargeable metal-ion batteries, Chemical Society Reviews, 49 (2020) 180–232.
11. Y. Zhuang, Q. Zong, Y. Wu, C. Liu, Q. Zhang, D. Tao, J. Zhang, J. Wang, G. Cao, Tuning [VO6] Octahedron of Ammonium Vanadates via F Incorporation for High-Performance Aqueous Zinc Ion Batteries, Small, 20 (2024) 2306561.
12. P. He, Y. Quan, X. Xu, M. Yan, W. Yang, Q. An, L. He, L. Mai, High-performance aqueous zinc–ion battery based on layered H2V3O8 nanowire cathode, Small, 13 (2017) 1702551.
13. M. Nadolska, M. Szkoda, K. Trzciński, J. Ryl, A. Lewkowicz, K. Sadowska, J. Smalc-Koziorowska, M. Prześniak-Welenc, New light on the photocatalytic performance of NH4V4O10 and its composite with rGO, Scientific Reports, 13 (2023) 3946.
14. Y. Cao, S. Ju, Q. Zhang, K. Gao, A. Marcelli, Z. Zhang, Recent progress in aqueous zinc-ion batteries based on conversion-type cathodes, Advanced Powder Materials, 4 (2025) 100278.
15. L. Chen, Z. Yang, Y. Huang, Monoclinic VO2(D) hollow nanospheres with super-long cycle life for aqueous zinc ion batteries, Nanoscale, 11 (2019) 13032–13039.
16. G. Li, Z. Yang, Y. Jiang, C. Jin, W. Huang, X. Ding, Y. Huang, Towards polyvalent ion batteries: A zinc-ion battery based on NASICON structured Na3V2(PO4)3, Nano Energy, 25 (2016) 211–217.
17. J. Hu, Y. Li, S. Shen, Y. Dong, D. Li, Y. Chen, Y. Fu, D. He, J. Li, Ammonium vanadate doped by transition bivalent metal ions for high-performance zinc-ion batteries, Journal of Electroanalytical Chemistry, 968 (2024) 118509.
18. Z. Deng, W. Shao, H. Wang, Y. Wang, J. Sheng, H. Mu, C. Lian, W. Wu, Augmenting specific capacitance of ammonium vanadate cathode in aqueous zinc-ion batteries via barium doping directed by glutamic acid, Journal of Power Sources, 614 (2024) 234976.
19. J. Cao, T. Ou, Y. Sun, H. Wu, D. Luo, C. Yang, L. Zhang, D. Zhang, X. Zhang, J. Qin, X. Yang, High-Rate and Ultra-Stable aqueous Zinc-Ion batteries enabled by Potassium-Infused ammonium vanadate nanosheets, Journal of Colloid and Interface Science, 665 (2024) 32–40.
20. R. Jia, C. Yin, J. Hu, Fabrication of NiCo-doped V2O5 nanospheres as cathode for enhanced Zn2 + storage performance, Colloids and Surfaces A: Physicochemical and Engineering Aspects, 727 (2025) 138186.
21. T. Zhou, G. Gao, Pre-intercalation strategy in vanadium oxides cathodes for aqueous zinc ion batteries: Review and prospects, Journal of Energy Storage, 84 (2024) 110808.

22. B. Zhang, Y. Jiang, S. Deng, X. Yan, Zincophilic and hydrophobic group grafting vanadyl phosphate cathode for high performance zinc ion batteries, Journal of Energy Storage, 114 (2025) 115873.
23. C. Deng, Y. Li, S. Liu, J. Yang, B. Huang, J. Liu, J. Huang, Nature-inspired interfacial engineering for highly stable Zn metal anodes, Energy Storage Materials, 58 (2023) 279–286.
24. X. Zhang, X. Ma, H. Bi, Y. Zhang, P. Mi, F. Liu, X. Jin, Y. Chen, K. Zhang, J. Wang, Y. Dong, Carboxymethylcellulose Induced the Formation of Amorphous MnO2 Nanosheets With Abundant Oxygen Vacancies for Fast Ion Diffusion in Aqueous Zinc-Ion Batteries, Advanced Functional Materials, 35 (2025) 2411990.
25. T. Liu, H. Yang, H. Fei, X. Yang, M. Li, Q. Deng, T. Liu, S. Hou, T. Huang, L. Zhao, Low-Content Mg2 + Preintercalation-Mediated Structural Stabilization in the NH4V4O10 Cathode Enables Ultrastable Zinc-Ion Storage, ACS Sustainable Chemistry & Engineering, 14 (2026) 3509–3521.
26. S. Grover, S. Goel, V. Sahu, G. Singh, R.K. Sharma, Asymmetric Supercapacitive Characteristics of PANI Embedded Holey Graphene Nanoribbons, ACS Sustainable Chemistry & Engineering, 3 (2015) 1460–1469.
27. Y. Ba, G. Yang, R. Jiang, J. Tang, Y. Xu, W. Liu, V2O5/Mesocarbon Microbeads Composites with Oxygen Vacancies as Cathodes for Sodium-Ion Batteries, Energy & Fuels, 40 (2026) 1778–1785.
28. R. Wang, H. Dai, T. Zhang, J. Zhou, L. Yin, J. Zhou, G. Sun, Heterostructure Design of Amorphous Vanadium Oxides@Carbon/Graphene Nanoplates Boosts Improved Capacity, Cycling Stability and High Rate Performance for Zn2 + Storage, Advanced Functional Materials, 35 (2025) 2421857.
29. J. Liu, M. Zheng, X. Shi, H. Zeng, H. Xia, Amorphous FeOOH Quantum Dots Assembled Mesoporous Film Anchored on Graphene Nanosheets with Superior Electrochemical Performance for Supercapacitors, Advanced Functional Materials, 26 (2016) 919–930.
30. X. Zheng, S.S. Mofarah, R.F. Webster, J. Zhang, C. Cazorla, Y. Nie, S. Wang, Y. Jiang, T. De Villenoisy, J. Wang, Y. Yao, T. Zhao, L. Dai, S.L.Y. Chang, C. Zhao, D. Chu, L. Sheppard, P. Koshy, C.C. Sorrell, Transforming disorder in the design of advanced high-entropy oxide electrocatalysts for zinc-air batteries, Nature Communications, 17 (2026) 3082.
31. B. Zhang, Y. Huang, S. Gao, N. Zhang, Y. Mei, Y. Huang, T. Ding, X. Hu, L. Li, F. Wu, R. Chen, Uncovering diverse roles of zincophilic and hydrophobic interactions at composite interfaces to enhance the longevity of zinc-ion batteries, Journal of Energy Chemistry, 107 (2025) 908–918.
32. P. Zou, R. Lin, T.P. Pollard, L. Yao, E. Hu, R. Zhang, Y. He, C. Wang, W.C. West, L. Ma, O. Borodin, K. Xu, X.-Q. Yang, H.L. Xin, Localized Hydrophobicity in Aqueous Zinc Electrolytes Improves Zinc Metal Reversibility, Nano Letters, 22 (2022) 7535–7544.
33. B.-B. Hu, D.-S. Li, H. Cheng, P.-P. Wang, X.-Y. Yang, M.-X. Li, H. Pu, G.-Q. Ma, C.-S. Li, Y. Sun, Z. Li, Organic molecules intercalated hydrated vanadium oxide with bifunctional of hydrophobicity and pillar in aqueous zinc-ion batteries, Rare Metals, 44 (2025) 7209–7219.
34. W. Wang, C. Yang, X. Chi, J. Liu, B. Wen, Y. Liu, Ultralow-water-activity electrolyte endows vanadium-based zinc-ion batteries with durable lifespan exceeding 30 000 cycles, Energy Storage Materials, 53 (2022) 774–782.

35. Y. Qiu, T. Chen, J. Zeng, Y. Tang, X. Wang, Interface strategies for long-term stability of manganese-based aqueous zinc-ion batteries, Environmental Surfaces and Interfaces, 4 (2026) 134–151.
36. T. Zhou, X. Du, G. Gao, Revealing the role of calcium ion intercalation of hydrated vanadium oxides for aqueous zinc-ion batteries, Journal of Energy Chemistry, 95 (2024) 9–19.

Figures

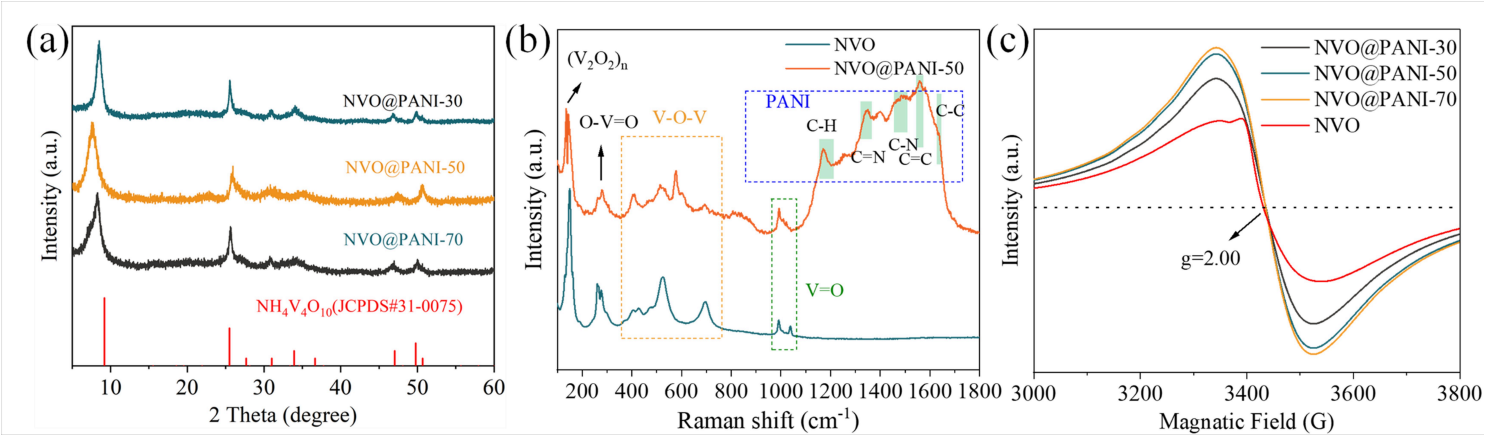


Figure 1

(a) XRD patterns of NVO@PANI-X; (b) Raman spectra of NVO@PANI-50 and bare NVO; (c) EPR spectra of NVO@PANI-X and bare NVO

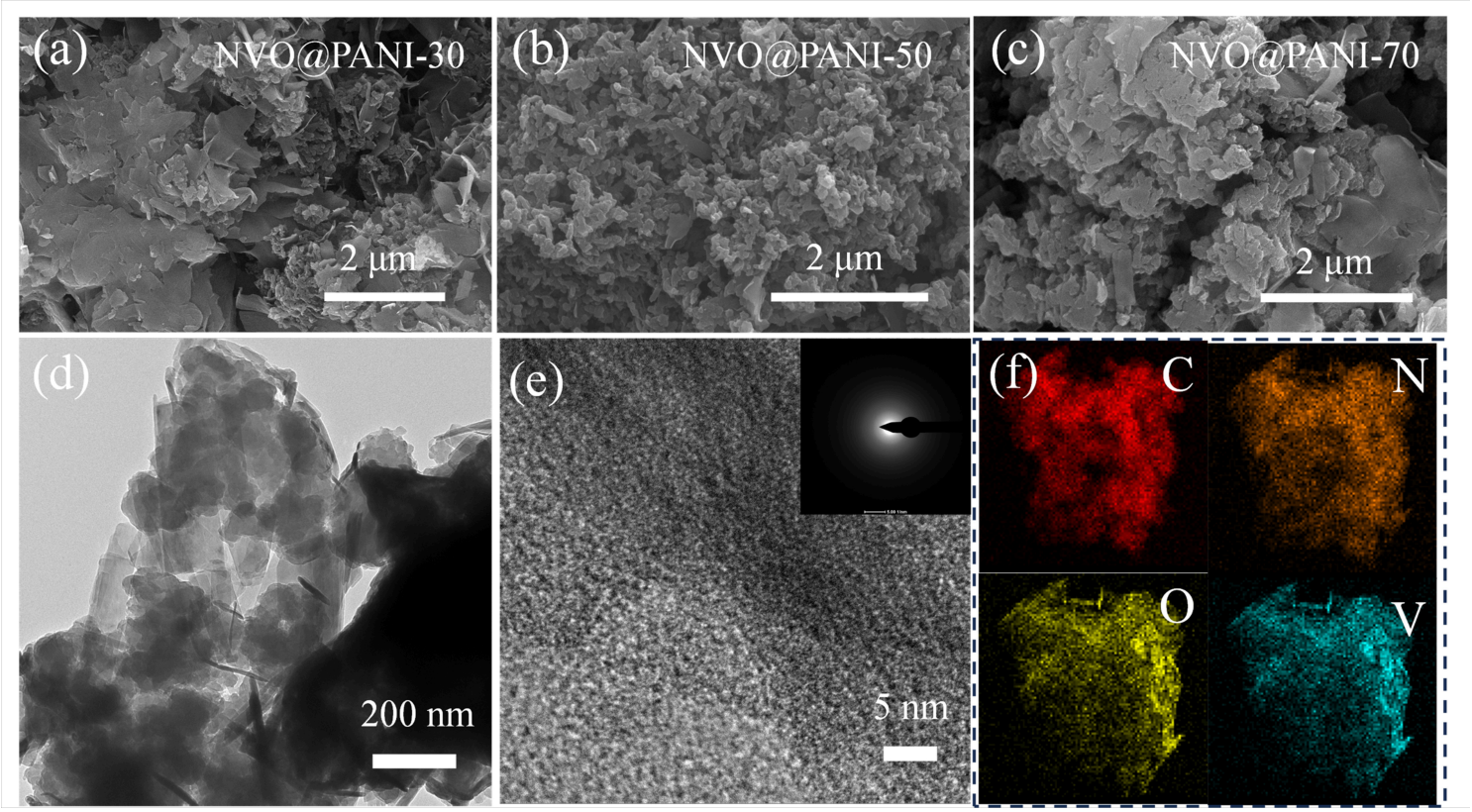


Figure 2

(a-c) SEM images of NVO@PANI-X; (d, e) TEM, HRTEM and SAED images of NVO@PANI-50; (f) EDS spectrum of NVO@PANI-50

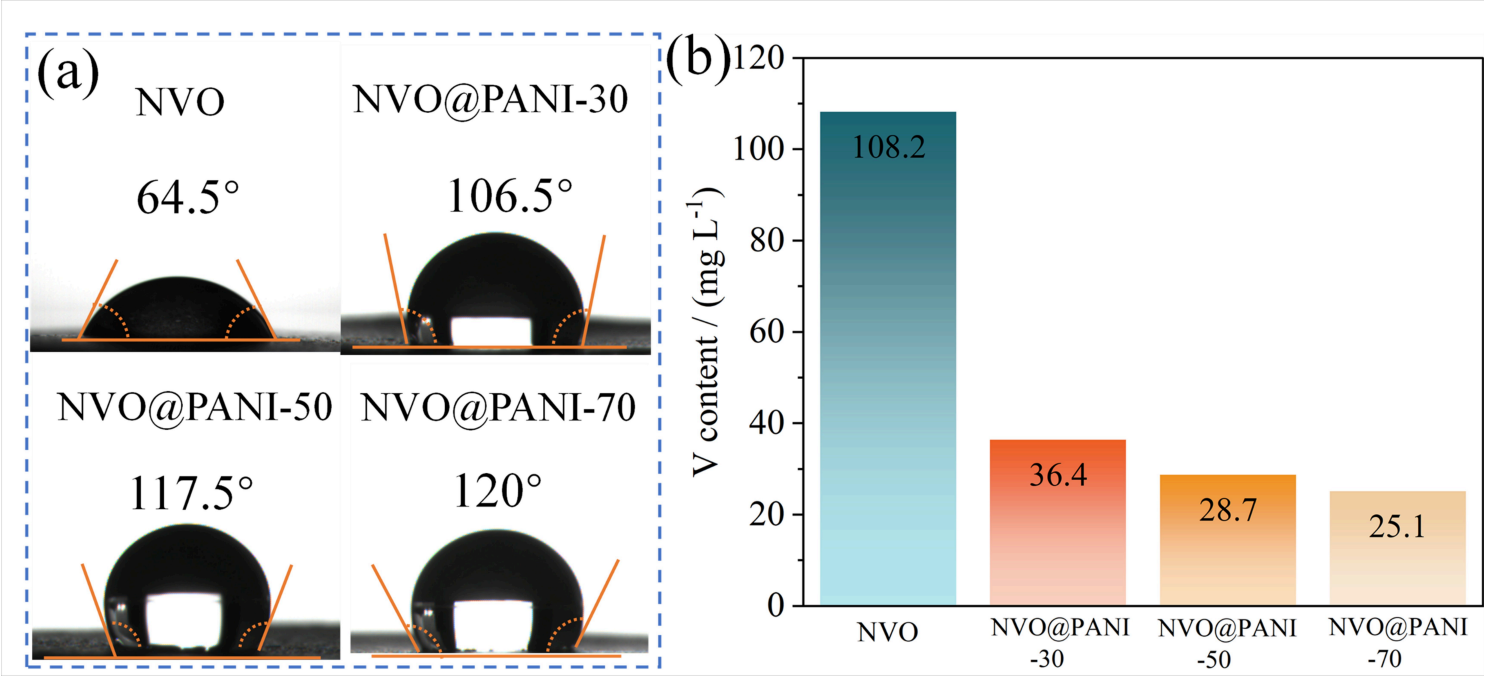


Figure 3

(a) Contact angle measurements of NVO and NVO@PANI-X; (b) Vanadium concentration in 3 M $Zn(OTF)_2$ electrolyte after 30-day immersion of NVO and NVO@PANI-X samples.

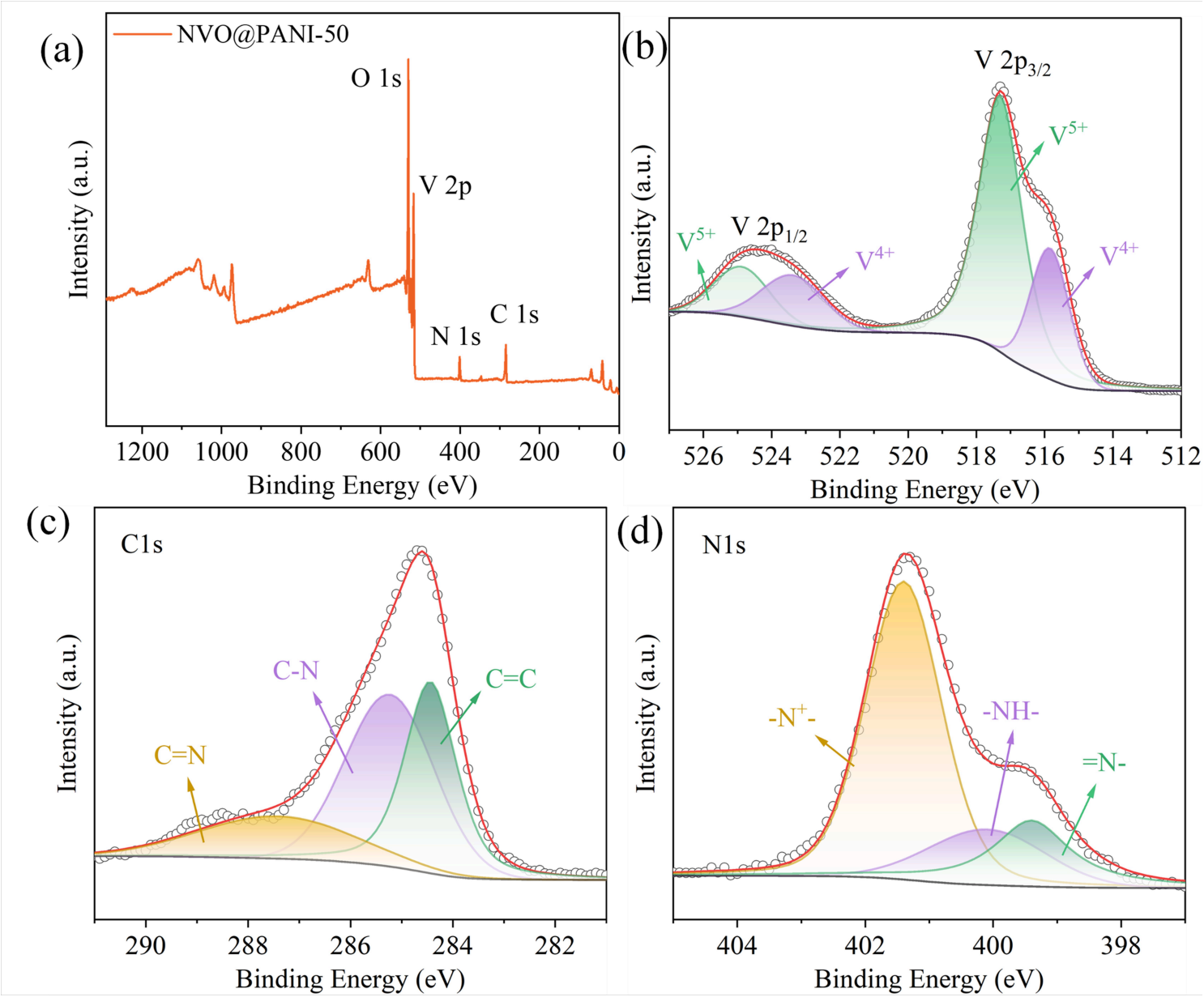


Figure 4

(a) Survey XPS spectra of NVO@PANI-50; (b-d) high-resolution V 2p, C 1s and N 1s spectra of NVO@PANI-50

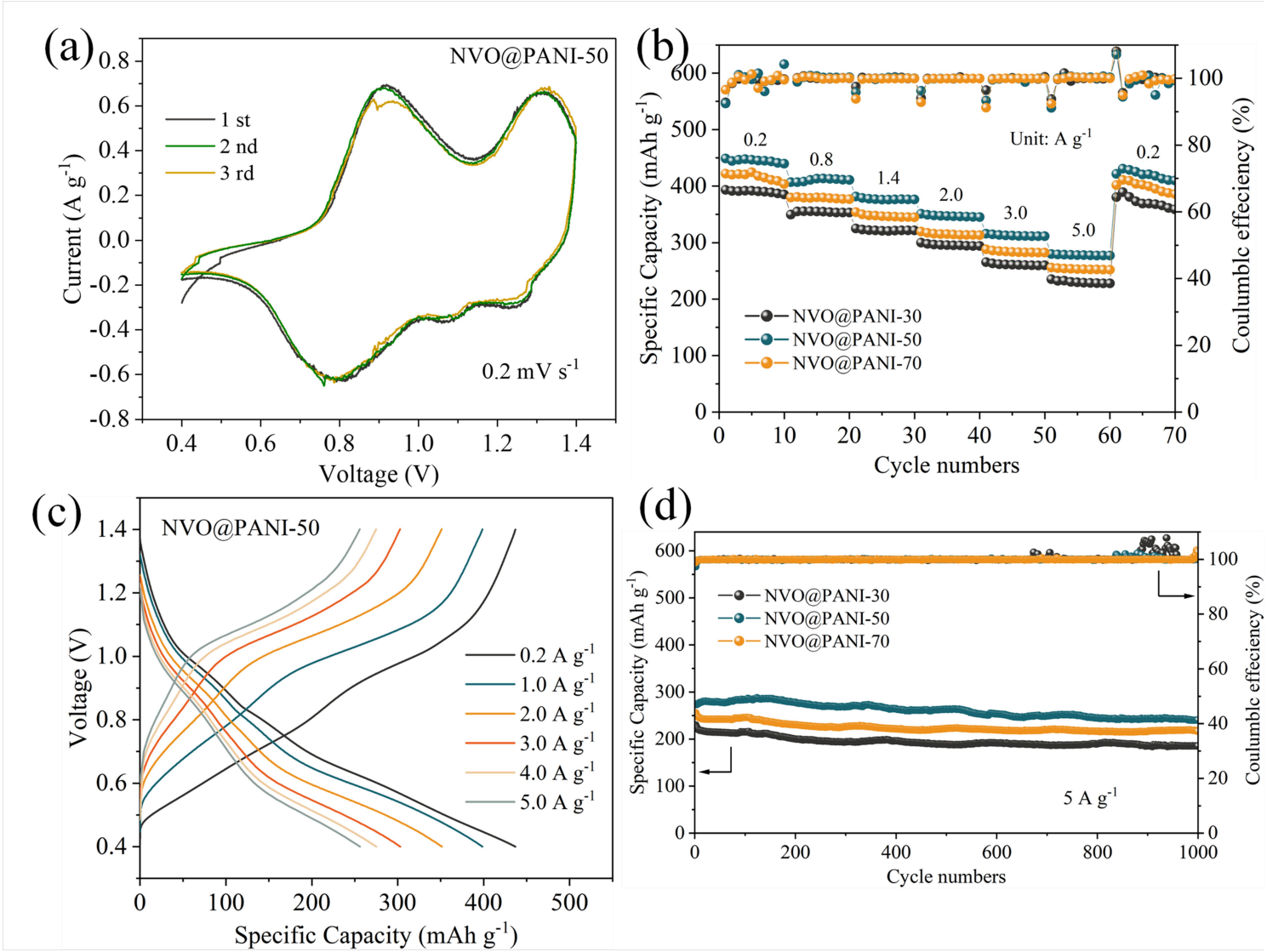


Figure 5

(a) CV curves at 0.2 mV s^{-1} for the initial three cycles and (b) GCD curves at different current densities of NVO@PANI-50 (c) Rate capability and (d) Cycling performance at 5 A g^{-1} of NVO@PANI-X.

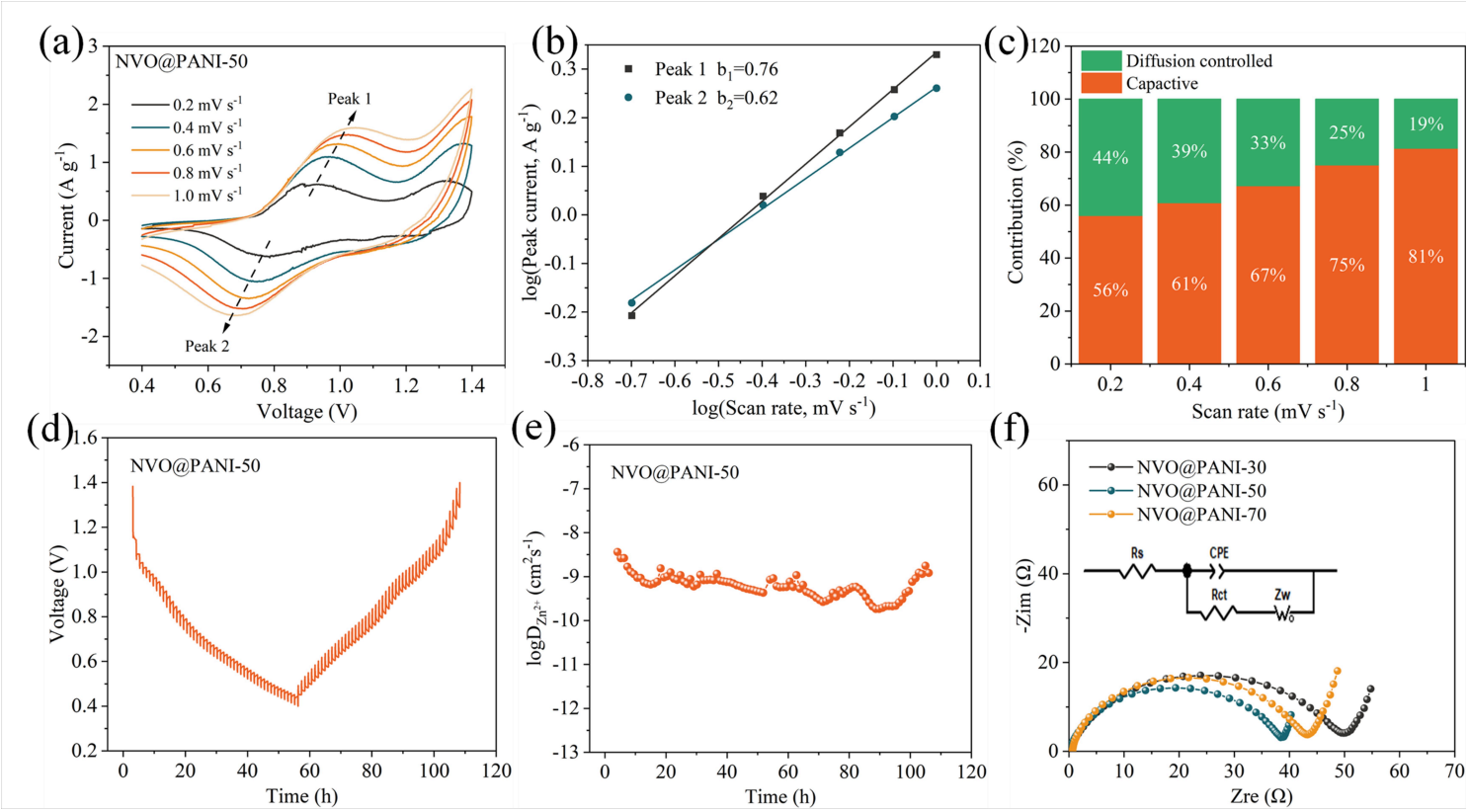


Figure 6

(a) CV curves at various scan rates, (b) log (i) vs. log v plot at specific peak currents, (c) surface-controlled at different scan rates, (d, e) GITT curves and Zn^{2+} diffusion coefficient calculations and (f) EIS Nyquist plots of NVO@PANI-X.

Supplementary Files

This is a list of supplementary files associated with this preprint. Click to download.

- supporttinginformation.docx